Science Advances
AAAS

Supplementary Materials for

Plasmonic linear nanomotor using lateral optical forces

Yoshito Y. Tanaka*, Pablo Albella, Mohsen Rahmani, Vincenzo Giannini, Stefan A. Maier, Tsutomu Shimura

*Corresponding author. Email: yoshito@iis.u-tokyo.ac.jp

The PDF file includes:

Other Supplementary Material for this manuscript includes the following:

Section S1. Unidirectional side scattering of light by an asymmetric nanorod pair

In the case of a single gold nanorod smaller than an illumination light wavelength, its far-field scattering patterns in xy plane and xz plane show a simple dipole radiation, as shown in fig. S3A. When we put another nanorod with different length, i.e., different phase of plasmon oscillation, the scattering patterns drastically change from the dipole radiation to unidirectional side scattering (fig. S3B). The directionality is determined by the distance d and phase difference $\Delta\Phi$ between the two nanorods, as shown in fig. S4. The retardation phase kd due to the propagation of their scattered light with wavenumber k can compensate $\Delta\Phi$ in one direction along the line connecting them and add up in the opposite direction.

Section S2. Translational and rotational friction coefficients

The friction coefficient f of a particle can be obtained from Einstein's relation (*37*):

$$f = \frac{k_B T}{D} \tag{1}$$

where D is the diffusion coefficient of the particle, $k_B T$ is the thermal energy, and k_B is the Boltzmann constant. The translational diffusion coefficient D_T is given from the mean squared translational displacement $\langle \Delta x^2 \rangle$ of the Brownian particle in time t (*37*):

$$D_T = \frac{\langle \Delta x^2 \rangle}{2t} \tag{2}$$

The rotational diffusion coefficient D_R is also described with the mean squared angular displacement $\langle \Delta \theta^2 \rangle$ (*37*):

$$D_R = \frac{\langle \Delta \theta^2 \rangle}{4t} \tag{3}$$

Therefore, the measurements of displacements Δx and $\Delta \theta$ in time t determine the translational and rotational friction coefficients, respectively. In order to estimate the lateral force on the rectangular microblock in Fig. 2, we measured the mean squared translational displacement of the Brownian block in its longitudinal direction and obtained the friction coefficient, f_T = 58

fN/μm·sec^{-1}. To derive the torque on the square block in Fig. 3D, we obtained its rotational friction coefficient, $f_R = 140$ pN·nm/rad·sec^{-1}.

Section S3. Optical force calculation with Maxwell stress tensor

The optical force acting on asymmetric nanorod pairs was calculated from the conservation law of linear momentum, which can be expressed as

$$\frac{d}{dt}\left(\boldsymbol{P}_{mech} + \boldsymbol{P}_{field}\right) = \oint_S \mathbf{T}_M \cdot \boldsymbol{n}\, dS \tag{4}$$

where $\boldsymbol{P}_{mech}$ is the mechanical momentum of the pairs, $\boldsymbol{P}_{field}$ is the momentum of the field, S is an arbitrary closed surface surrounding the pairs, and $\boldsymbol{n}$ is the outward normal to its surface. $\mathbf{T}_M$ is Maxwell stress tensor (MST), which is defined as

$$\mathbf{T}_M = \varepsilon E \otimes E + \frac{1}{\mu} B \otimes B - \frac{1}{2}\left(\varepsilon E \cdot E + \frac{1}{\mu} B \cdot B\right)\mathbf{I} \tag{5}$$

where ε and μ are the permittivity and permeability of the surrounding medium. $\otimes$ denotes the operation of dyadic product. $\mathbf{I}$ is the unit dyadic. E and B are the electric and magnetic field. The right-hand side of Eq. (4) represents the flux of linear momentum that enters the surface S. The time derivative of the field linear momentum is zero when it is averaged over one oscillation period. Therefore, the time-averaged mechanical force on the pairs can be obtained by

$$F = \oint_S \mathbf{T}_M \cdot \boldsymbol{n}\, dS \tag{6}$$

Section S4. Plasmonic heating effects

Since heating is intrinsic to gold nanoparticles supporting localized plasmon resonances, it may give rise to an undesired fluid motion that affects or interfere with the motor motion. In particular, the presence of temperature gradient imposes thermophoretic force on a particle, which pushes the particle from regions of high temperature to low. Fig. S5 shows calculated temperature

distributions of a silica microblock containing a single motor. We used a finite element method solver (Comsol) for the simulation of a model in fig. S5A. A plane wave (the intensity of 0.4 mW/μm^2 and wavelength of 910 nm used in the experiment) excites a plasmon resonance of the motor. The temperature is concentrically distributed around the motor, and the maximum temperature rises on the motor, the top and side walls of the block are about 4.5, 1.5 and 0.5 degrees, respectively, as shown in fig. S5B. For the sample of the linear nanomotors in Fig. 2, the maximum temperature rise on the motors, the top and side walls of the block can be estimated to be less than 10, 3 and 1 degrees, respectively, from the temperature rise on the individual motors and the heat transfer function in the silica block. Some previous studies report that the temperature rise less than 5 degrees on a gold microdisk in water by a plasmon excitation leads to a maximum fluid velocity on the order of 1 nm/s (38, 39). This thermally induced fluid convection is much slower than the measured velocity of the linear motor, 6.8 μm/s. Furthermore, since our nanomotors are periodically arranged in the center of the microblock, the temperature should be symmetrically distributed on the block surface. Thus, the thermophoretic forces on the side walls, arising from collisions between the water molecules and the block surface, can be canceled each other out. These indicate that the plasmonic heating effect is negligible for the motion of the motors in our study.

Section S5. Rotational behavior with symmetric nanorod pairs

In order to confirm that the directional rotation in Fig. 3D stems from neither the plasmonic heating effect and the surface roughness of the microblock, the rotational behavior of the microblock with symmetric nanorod pairs in fig. S6A has been analyzed. The dimension and material of the block are the same as those in Fig. 3C. The nanorod pairs have a single plasmon resonance at a wavelength of 910 nm, corresponding to the illumination wavelength, as shown in fig. S6B. Fig. S6 (C and D) show that the sample does not rotate in one direction under the same illumination condition as Fig. 3D. In other words, slightly different nanorod lengths produce the

obvious difference of the rotational behavior. This strongly supports that the directional rotation is a result of torque generated by the lateral force due to the unidirectional side scattering by the asymmetric nanorod pair.

Section S6. Directivity of scattered light from an asymmetric nanorod pair

Fig. S7 shows the dependence of the directivity of the scattered light on the illumination wavelength in relation with the extinction spectrum in Fig. 1B. The directivity of the scattered light is defined as the ratio of the intensity between two diametrically opposite angular regions, i.e., $\varphi = 0°$ and $180°$ in Fig. 1C. The directivity peak is just between the two resonances because here we have the ideal interfering situation of both nanorods radiating with almost the same power.
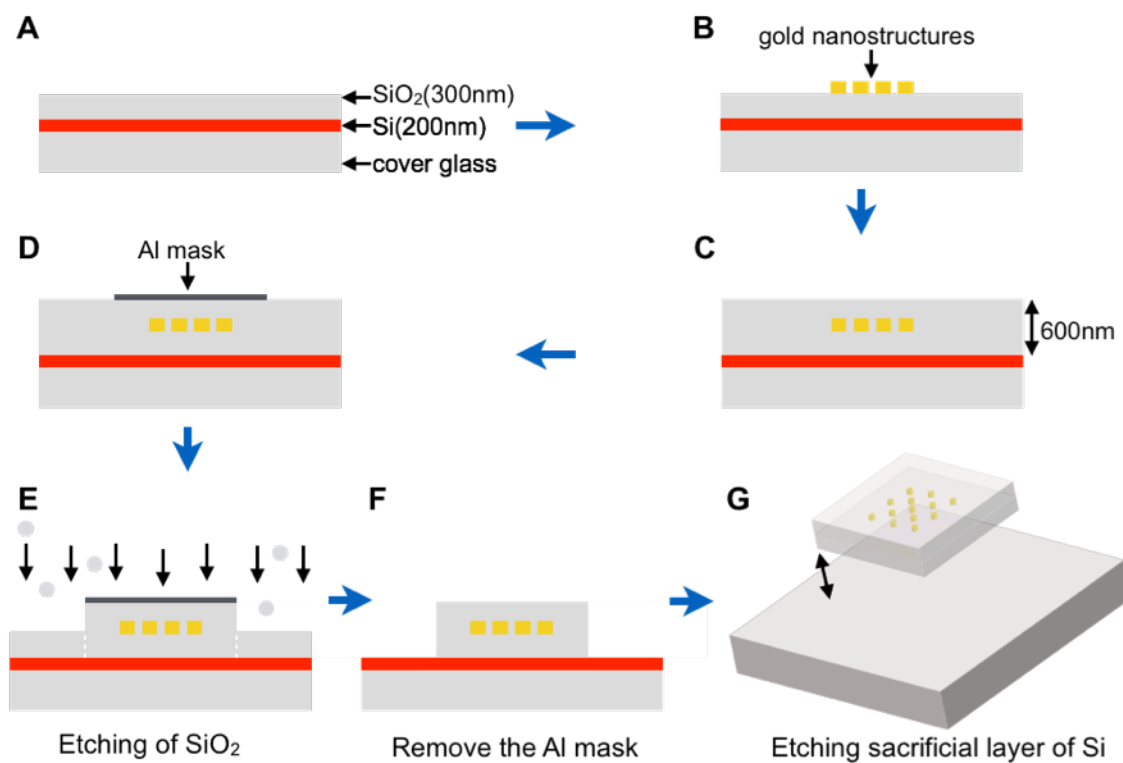
Fig. S1. Fabrication process. **(A)** A Si layer and a SiO_2 layer were deposited on a coverslip substrate by sputtering. **(B)** Gold nanostructures were fabricated using electron beam lithography (EBL). **(C)** Additional sputtering of a SiO_2 layer sandwiched the nanostructures. **(D)** A second EBL fabricated an Al etching mask. **(E)** Etching of SiO_2 shaped a microblock. **(F** and **G)** After removing the mask and the sacrificed layer of Si, the sample can be released from the substrate.
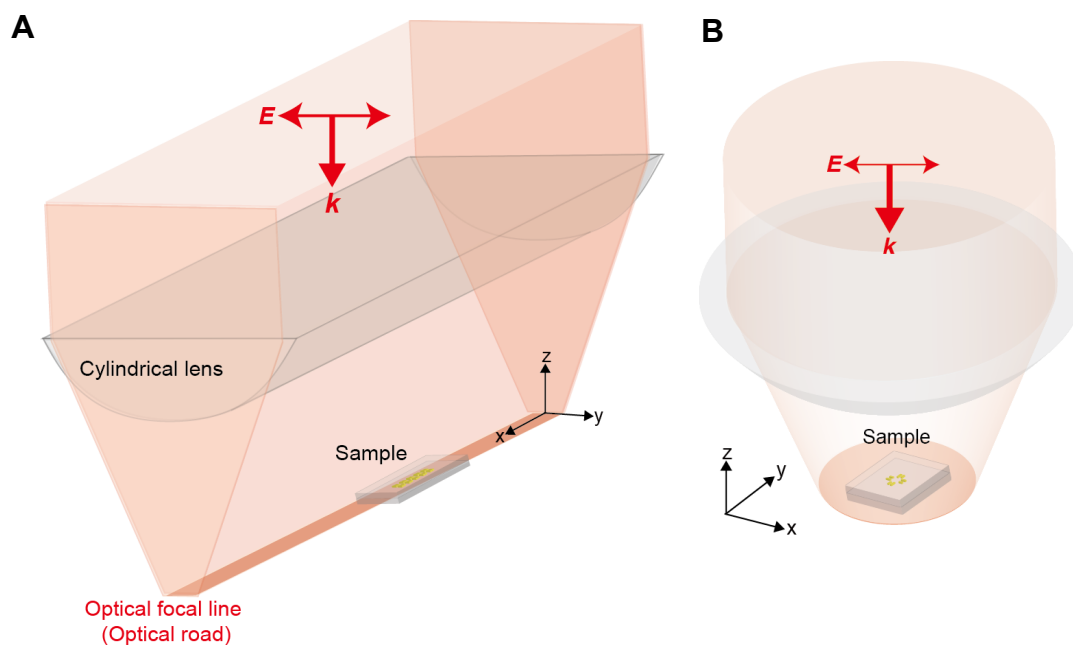
Fig. S2. Light illuminations of the samples. The samples were illuminated by a linearly polarized beam at the normal incidence from the top. **(A)** For the experiment of linear movement, the optical focal line to confine and align the sample was generated by a cylindrical lens. **(B)** For the experiment of the sample rotation, the laser beam was weakly focused with a larger spot size than the sample to obtain uniform illumination.
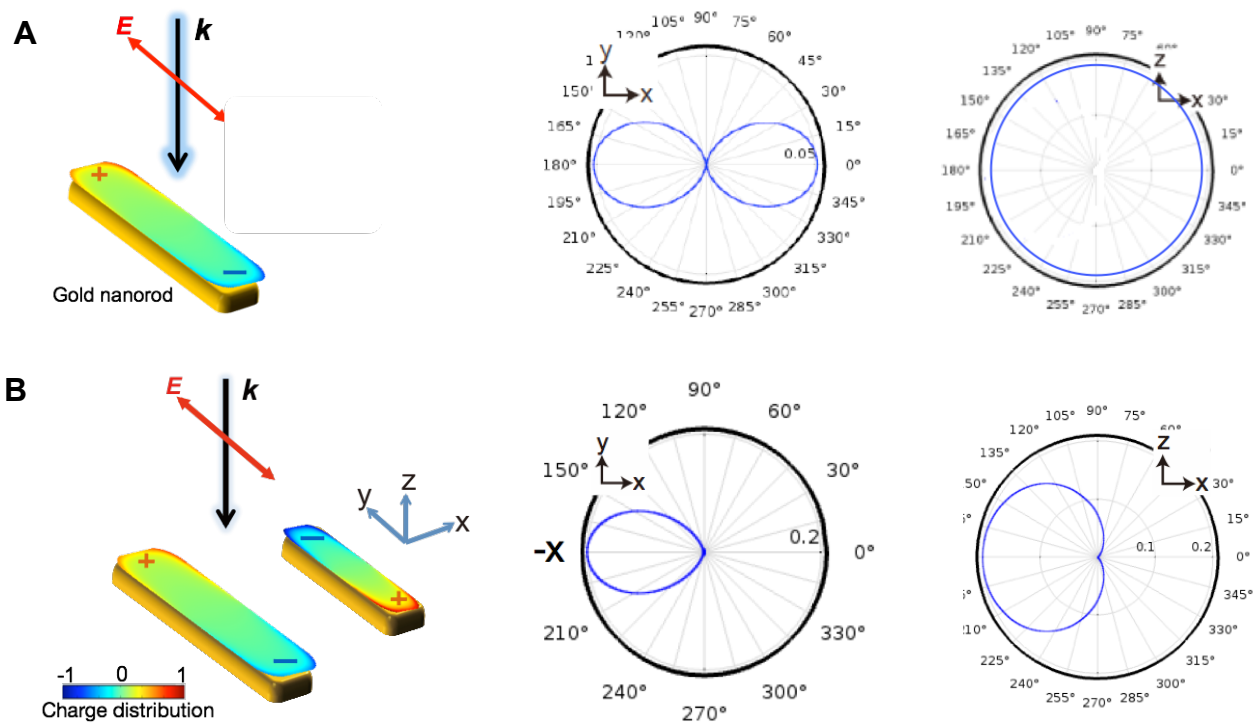
Fig. S3. Caluculated far-field scattering patterns: (**A**) a single nanorod and (**B**) an asymmetric nanorod pair embedded in silica glass. The scattering patterns drastically change from the dipole radiation to unidirectional side scattering.
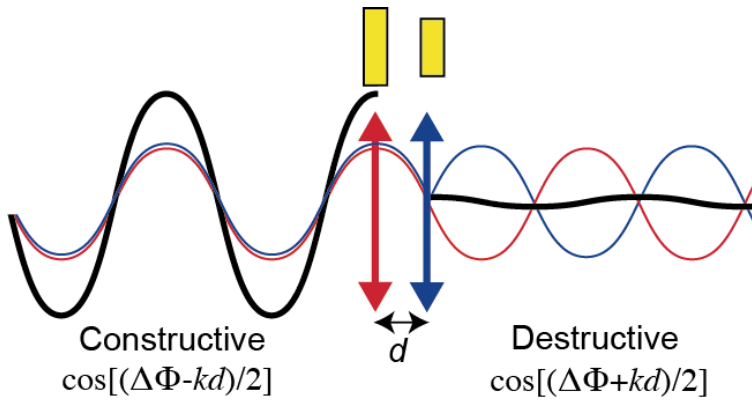
Constructive
$\cos[(\Delta\Phi - kd)/2]$

d

Destructive
$\cos[(\Delta\Phi + kd)/2]$

Fig. S4. Directional scattering from two dipole sources. When two dipoles separated by a distance d have the phase difference $\Delta\Phi$, there are the asymmetric interferences between their radiation fields in right and left directions, constructive interference in one direction and destructive interference in the other.
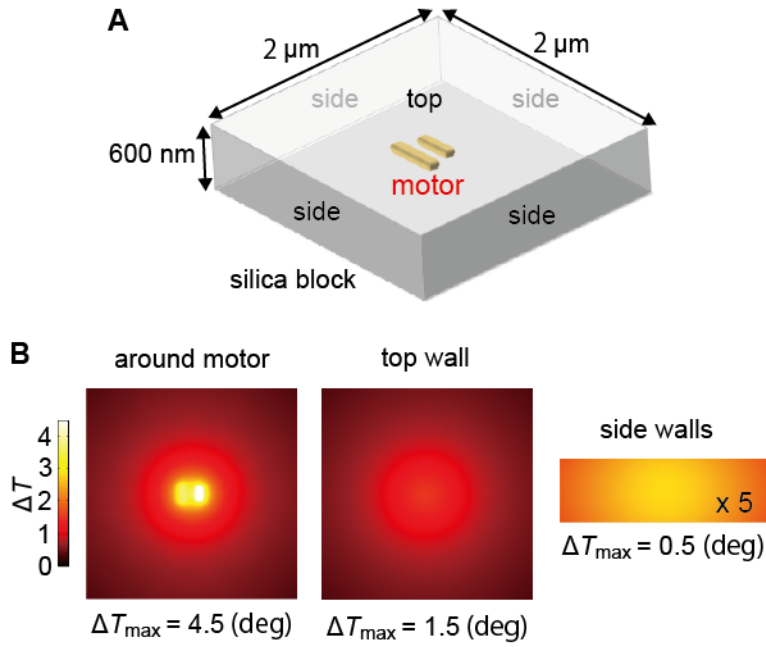
Fig. S5. Calculated temperature distribution of a silica microblock containing a motor. (A) A simulation model. A 600-nm-thick, 2 μm x 2 μm silica block contains a single nanomotor in its centre. The microblock is surrounded by water. (**B**) Temperature distributions on the motor and the top and side walls of the block under the normal incidence of a linearly polarized plane wave for the intensity of 0.4 mW/μm^2 and wavelength of 910 nm, which we used in the experiments of Fig.2. The illumination light polarization is parallel to the rod axis. The temperature is symmetrically distributed around the motor. The maximum temperature rises on the motor, the top and side walls of the block are about 4.5, 1.5 and 0.5 degrees, respectively.
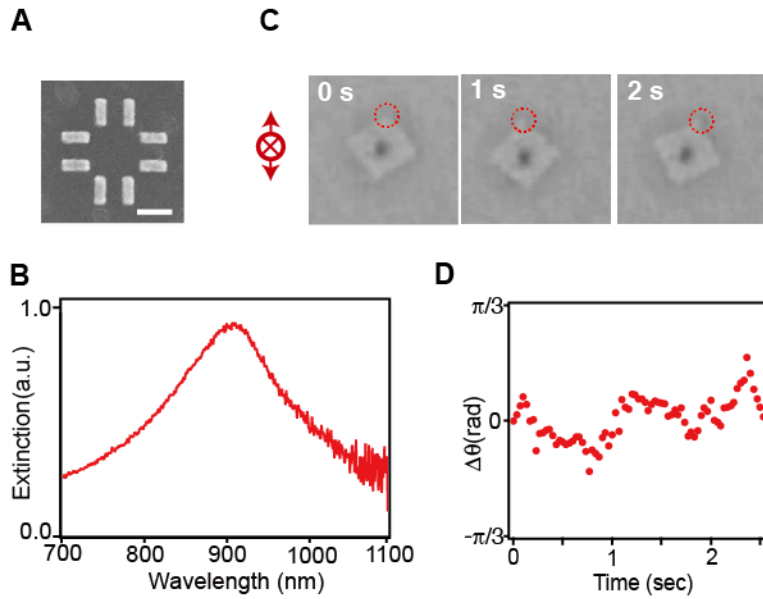
Fig. S6. Experimental characterization of rotational behavior with symmetric nanorod pairs. (A) SEM image of a circular array of symmetric nanorod pairs. Scale bar is 200 nm. **(B)** Extinction spectrum of the pairs embedded in silica glass. **(C)** Time sequence of optical microscopy images of a sample in water under the normal incidence of a linearly polarized light (wavelength of 910 nm, the intensity of 4.5 mW/μm²). The sample is a 600-nm-thick, 2.5 μm x 2.5 μm square silica block containing the pairs. The dashed red circles indicate the same corner of the block. **(D)** Rotational dynamics of the sample.
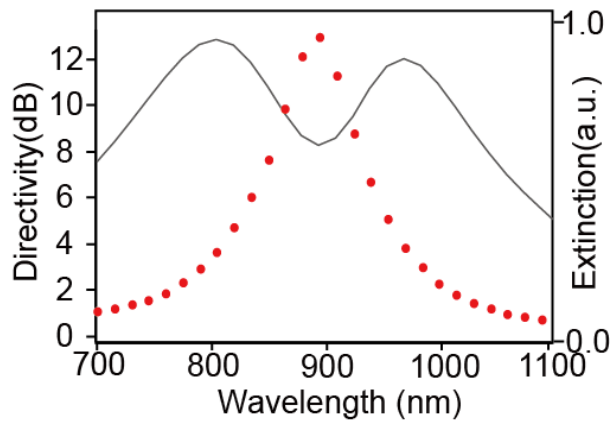
Fig. S7. Calculated wavelength dependence of directivity of the scattered light. The red dots and a gray curve show the directivity and extinction cross-section, respectively, of an asymmetric nanorod pair embedded in silica glass. The directivity of the scattered light is defined as the ratio of the intensity between two diametrically opposite angular regions, i.e., $\varphi = 0°$ and $180°$ in Fig. 1C. The nanorod pair embedded in silica glass exhibits strong lateral directionality at the central wavelength between two dipolar resonances.

Movies (S1-S4) Captions

Movie S1. Linear movement produced by a linear array of the nanomotors. The sample was illuminated by a linearly polarized beam at the normal incidence. An optical focal line generated using a cylindrical lens can confine and align the sample along its line axis. The sample travels along the line axis perpendicular to the incident light direction. It should be noted that the illumination light beam carries the linear momentum in its incident direction only, with a zero lateral component in the line axis direction.

Movie S2. Polarization switching of the linear movement. For the polarization direction along the nanorod axis, the sample travels along the optical road. When the polarization is rotated by 90° at ~ 2 s, while keeping the light intensity constant, the linear movement stops quickly. The video after the polarization rotation can be seen to be slightly brighter than before, because of differential reflectivity of a dichroic mirror on front of an imaging CMOS camera.

Movie S3. Rotational movement produced by a circular array of the nanomotors with separation of 290 nm. A linearly polarized beam was weakly focused with a larger spot size than the sample to obtain uniform illumination. The sample rotates in an anticlockwise direction under the illumination of light without angular momentum.

Movie S4. Rotational movement produced by a circular array of the nanomotors with separation of 1340 nm. The sample rotates at double speed with less than half of the light intensity, while keeping the whole volume of the nanoparticles.

REFERENCES AND NOTES

1. J. Glückstad, Microfluidics: Sorting particles with light. *Nature Mater.* **3**, 9–10 (2004).

2. S. Maruo, H. Inoue, Optically driven micropump produced by three-dimensional two-photon microfabrication. *Appl. Phys. Lett.* **89**, 144101 (2006).

3. S. Maruo, H. Inoue, Optically driven viscous micropump using a rotating microdisk. *Appl. Phys. Lett.* **91**, 084101 (2007).

4. A. Terray, J. Oakey, D. W. M. Marr, Microfluidic control using colloidal devices. *Science* **296**, 1841–1844 (2002).

5. S. L. Neale, M. P. Macdonald, K. Dholakia, T. F. Krauss, All-optical control of microfluidic components using form birefringence. *Nat. Mater.* **4**, 530–533 (2005).

6. S. Kawata, H.-B. Sun, T. Tanaka, K. Takada, Finer features for functional microdevicecs. *Nature* **412**, 697–698 (2001).

7. D. G. Grier, A revolution in optical manipulation. *Nature* **424**, 810–816 (2003).

8. D. Palima, J. Glückstad, Gearing up for optical microrobotics: Micromanipulation and actuation of synthetic microstructures by optical forces. *Laser Photon. Rev.* **7**, 478–494 (2013).

9. U. G. Būtaitė, G. M. Gibson, Y.-L. D. Ho, M. Taverne, J. M. Taylor, D. B. Phillips Indirect optical trapping using light driven micro-rotors for reconfigurable hydrodynamic manipulation. *Nat. Commun.* **10**, 1215 (2019).

10. H. Xu, M. Käll, Surface-plasmon-enhanced optical forces in silver nanoaggregates. *Phys. Rev. Lett.* **89**, 246802 (2002).

11. P. M. Hansen, V. K. Bhatia, N. Harrit, L. Oddershede, Expanding the optical trapping range of gold nanoparticles. *Nano Lett.* **5**, 1937–1942 (2005).

12. Y. Tanaka, H. Yoshikawa, T. Itoh, M. Ishikawa, Laser-induced self-assembly of silver nanoparticles via plasmonic interactions. *Opt. Express* **17**, 18760–18767 (2009).

13. M. J. Guffey, R. L. Miller, S. K. Gray, N. F. Scherer, Plasmon-driven selective deposition of Au bipyramidal nanoparticles. *Nano Lett.* **11**, 4058–4066 (2011).

14. A. Lehmuskero, P. Johansson, H. Rubinsztein-Dunlop, L. Tong, M. Käll, Laser trapping of colloidal metal nanoparticles. *ACS Nano* **9**, 3453–3469 (2015).

15. A. H. J. Yang, T. Lerdsuchatawanich, D. Erickson, Forces and transport velocities for a particle in a slot waveguide. *Nano Lett.* **9**, 1182–1188 (2009).

16. S. Kawata, T. Tani, Optically driven Mie particles in an evanescent field along a channeled waveguide. *Opt. Lett.* **21**, 1768–1770 (1996).

17. M. Ploschner, T. Čižmár, M. Mazilu, A. Di Falco, K. Dholakia, Bidirectional optical sorting of gold nanoparticles. *Nano Lett.* **12**, 1923–1927 (2012).

18. K. Wang, E. Schonbrun, K. B. Crozier, Propulsion of gold nanoparticles with surface plasmon polaritons: Evidence of enhanced optical force from near-field coupling between gold particle and gold film. *Nano Lett.* **9**, 2623–2629 (2009).

19. J.J. Sáenz Optical forces: Laser tractor beams. *Nat. Photon.* **5**, 514–515 (2011).

20. G. A. Swartzlander Jr., T. J. Peterson, A. B. Artusio-Glimpse, A. D. Raisanen, Stable optical lift. *Nat. Photon.* **5**, 48–51 (2011).

21. A. Búzás, L. Kelemen, A. Mathesz, L. Oroszi, G. Vizsnyiczai, T. Vicsek, P. Ormos, Light sailboats: Laser driven autonomous microrobots. *Appl. Phys. Lett.* **101**, 041111 (2012).

22. S. B. Wang, C. T. Chan, Lateral optical force on chiral particles near a surface. *Nat. Commun.* **5,** 3307 (2014).

23. F. J. Rodríguez-Fortuño, N. Engheta, A. Martínez, A. V. Zayats, Lateral forces on circularly polarizable particles near a surface. *Nat. Commun.* **6**, 8799 (2015).

24. T. Kosako, Y. Kadoya, H. F. Hofmann, Directional control of light by a nano-optical Yagi–Uda antenna. *Nat. Photon.* **4**, 312–315 (2010).

25. A. B. Evlyukhin, S. I. Bozhevolnyi, A. Pors, M. G. Nielsen, I. P. Radko, M. Willatzen, O. Albrektsen, Detuned electrical dipoles for plasmonic sensing. *Nano Lett.* **10**, 4571–4577 (2010).

26. M. Liu, T. Zentgraf, Y. Liu, G. Bartal, X. Zhang, Light-driven nanoscale plasmonic motors. *Nat. Nanotechnol.* **5**, 570–573 (2010).

27. L. Shao, Z.-J. Yang, D. Andrén, P. Johansson, M. Käll, Gold nanorod rotary motors driven by resonant light scattering. *ACS Nano* **9**, 12542–12551 (2015).

28. A. Lehmuskero, R. Ogier, T. Gschneidtner, P. Johansson, M. Käll, Ultrafast spinning of gold nanoparticles in water using circularly polarized light. *Nano Lett.* **13**, 3129–3134 (2013).

29. L. Shao, M. Käll, Light-driven rotation of plasmonic nanomotors. *Adv. Funct. Mater.* **28**, 1706272 (2018).

30. T. Shegai, S. Chen, V. D. Miljković, G. Zengin, P. Johansson, M. Käll, A bimetallic nanoantenna for directional colour routing. *Nat. Commun.* **2**, 481 (2011).

31. P. Albella, T. Shibanuma, S. A. Maier, Switchable directional scattering of electromagnetic radiation with subwavelength asymmetric silicon dimers. *Sci. Rep.* **5**, 18322 (2015).

32. J. Li, N. Verellen, D. Vercruysse, T. Bearda, L. Lagae, P. V. Dorpe, All-dielectric antenna wavelength router with bidirectional scattering of visible light. *Nano Lett.* **16**, 4396–4403 (2016).

33. R. Guo, M. Decker, F. Setzpfandt, I. Staude, D. N. Neshev, Y. S. Kivshar, Plasmonic Fano Nanoantennas for on-chip separation of wavelength-encoded optical signals. *Nano Lett.* **15**, 3324–3328 (2015).

34. Y. Y. Tanaka, T. Shimura, Tridirectional polarization routing of light by a single triangular plasmonic nanoparticle. *Nano Lett.* **17**, 3165–3170 (2017).

35. N. I. Zheludev, Y. S. Kivshar, From metamaterials to metadevices. *Nat. Mater.* **11**, 917–924 (2012).

36. C. Si, Z. Sun, F. Liu, Strain engineering of graphene: A review. *Nanoscale* **8**, 3207–3217 (2016).

37. A. P. Philipse, *Brownian Motion: Elements of Colloid Dynamics* (Springer, 2018).

38. J. S. Donner, G. Baffou, D. McCloskey, R. Quidant, Plasmon-assisted optofluidics. *ACS Nano* **5**, 5457–5462 (2011).

39. G. Baffou, R. Quidant, C. Girard, Thermoplasmonics modeling: A Green's function approach. *Phys. Rev. B* **82**, 165424 (2010).